Flow-Field Measurement of Embedded Streamwise Vortex Generated from Passive Flow-Control Devices

Chung-Sheng Yao, John C. Lin, and Brian G. Allan
NASA Langley Research Center
Flow Physics and Control Branch,
Mail Stop 170
Hampton, VA 23681-2199, USA
c.s.yao@nasa.gov

Abstract
Detailed flow-field measurements were performed downstream of a single vortex generator (VG) using a Stereo Digital Particle Image Velocimetry system. The passive flow-control devices examined consisted of a low-profile VG with a device height, h, approximately equal to 20 percent of the boundary-layer thickness, δ, and a conventional VG with h ≈ δ. Flow-field data were taken at twelve cross-flow planes downstream of the VG to document and quantify the evolution of embedded streamwise vortex. Key parameters including vorticity, circulation, trajectory, and half-life radius—describing concentration, strength, path, and size, respectively—of the device-induced streamwise vortex were extracted from the flow-field data. Peak vorticity and circulation for the low-profile VG decayed exponentially to the distance downstream from the device. The device-height normalized vortex trajectories for the low-profile VG, especially in the lateral direction, followed the general trends of the conventional VG.

1. INTRODUCTION

Flow-separation control remains extremely important for many technological applications of fluid mechanics because of the large energy losses often associated with boundary-layer separation. Controlling flow separation can result in an increase in system performance with consequent energy conservation as well as weight and space savings. In addition, properly applied flow control can also provide an expanding degree of freedom in the design optimization process.

For various separation-control applications, conventional vortex generators (VGs) first introduced by Taylor [1] have long been successfully used to increase near-wall momentum through enhanced momentum transfer from the outer flow to the wall region via streamwise vortices [2,3]. The VGs used in these studies generally consisted of a row of small vanes with device height, h, on the order of the boundary-layer thickness, δ, normal to the surface and set at an angle of incidence to the local flow to produce an array of streamwise trailing vortices. However, for some flow-control applications, the use of these relatively large, δ-scale VGs could cost excess residual drag through conversion of an aircraft's forward momentum into unrecoverable turbulence in its wake.

One method of improving the system efficiency is to generate an embedded streamwise vortex using minimal near-wall protuberances through substantially reduced device height. Lin et al. [4] showed that by reducing the height of conventional VGs to only a fraction of δ, the VGs could still provide effective momentum transfer towards the wall at a distance several times their own height, especially in turbulent boundary layers where the velocity profile is relatively full.

Holmes et al. [5] suggested that the low-profile VGs roughly follow many of the same guidelines established by Pearcey [3] for conventional VGs. The downstream effective distance, defined as a multiple of δ for the conventional VGs, shall be replaced by a multiple of h for the low-profile VGs instead. Consequently, the physical length of downstream effective distance, typically between about 5h to 30h, is thereby reduced due to the lower h.

These low-profile (sub-δ-scale) vortex generators, because of their small size, are referred to as micro-vortex generators (MVGs) [6,7], sub-boundary layer vortex generators (SBVGs) [8,9], and microvanes [10]. The MVGs were successfully used on multi-element high-lift airfoils to control flow separation on the flap where a significant performance enhancement of over 100 percent increase in

L/D was reported [6]. The MVGs were also the most effective devices in controlling separation that was dominated by a pair of junction vortices for flows over a backward-facing ramp [7]. Research at DERA successfully delayed the shock-induced separation on a transonic airfoil using the SBVGs, resulting in a 20% increase in maximum lift [8]. In addition, investigations were successfully conducted to suppress flow unsteadiness and distortion at the engine face inside compact inlet ducts of high-speed aircraft using the microvanes [10,11]. The engine-face flow distortion was attributed to local flow separation and unsteady secondary flow within the inlet ducts. The experimental study of Hamstra et al. [10] indicated that small microvanes, with the device height on the order of the boundary-layer momentum thickness, could increase the pressure recovery by up to 5% and reduce both spatial distortion and turbulence by as much as 50% inside an ultra-compact serpentine duct.

The success of using low-profile vortex generators such as MVGs, SBVGs, and microvanes for performance enhancement of various aerodynamics applications led to an increased interest in obtaining detailed flow-field information downstream of these devices for CFD development and a better understanding of related flow physics [8, 9]. Although there are some flow-field data available for the conventional VG [12–14], the experimental data on the developmental characteristics of an embedded streamwise vortex produced by the low-profile VG located within a turbulent boundary layer are particularly lacking. Furthermore, in order to develop simplified models for active (unsteady) flow-control devices—such as pulsed jets, synthetic jets, or pulsed vortex generator jets—for future applications, one must first be able to predict accurately and reliably the flow from a steady lowprofile VG. The experimental data presently available to validate these predictions are very limited.

Thus, the objectives of the current investigation were twofold:

(a) Provide the experimental database for the flow-field containing an embedded streamwise vortex downstream of a VG to validate the design tools.
(b) Gain a better understanding of flow physics associated with the device-induced vortex within a turbulent boundary layer.

2. EXPERIMENTAL APPARATUS

The detailed flow measurements were conducted in the Langley 20- by 28-Inch Shear Flow Tunnel at a free-stream velocity of 34 m/s. A 12.7-mm thick splitter plate was mounted 102 mm above the original test section floor to bypass the converging section boundary layer to eliminate any upstream influence. The new boundary layer on the splitter plate was immediately tripped with a 51-mm wide strip of sandpaper (36 grit). A single VG was located approximately 2.25 m downstream of the boundary-layer trip. At the device location, the boundary-layer thickness (δ) was approximately 35 mm.

A rectangular vane-type low-profile VG with a height of 7 mm ($h/\delta \approx 0.20$) and a device length, e, of 49 mm ($e/h = 7$) was chosen for this test. Three device angles of attack (α's) of 10°, 16°, and 23° were selected, which covers a nominal range of effective α. In addition to the low-profile VG, a conventional VG with a height of 35 mm ($h/\delta \approx 1.0$) and a length of 70 mm ($e/h = 2$) was also tested at the same three angles of attack for comparison. The geometry of both VGs is illustrated in Figure 1. For time and resource considerations, decisions were made to narrow the VG parameters examined.

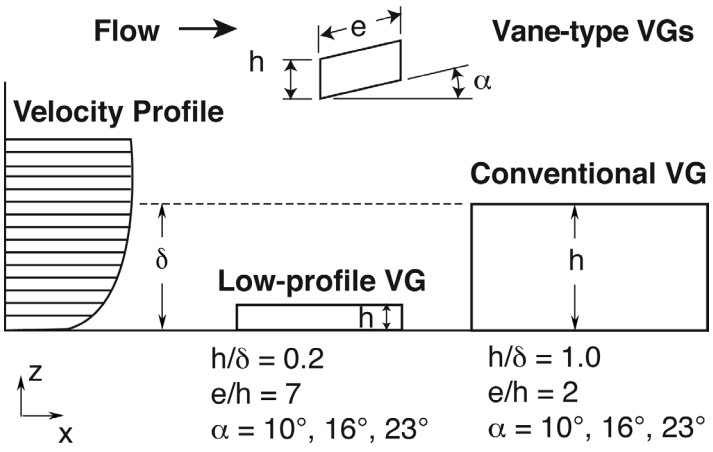

Figure 1. Geometry of VG examined.

The rectangular shape was chosen for the VG in order to investigate only the effect of device height and aspect ratio, eliminating the effect of the device's (leading-edge) sweep angle. Because there is a lack of existing data for using VGs with $\alpha > 23°$ in practical applications, the maximum α was limited to 23° in this study.

A Stereo Digital Particle Image Velocimetry (SDPIV) system was used to provide rapid flow-field measurements downstream of the VG. The system consisted of a frequency-doubled, 120mJ Nd:YAG laser operating at 15 Hz that illuminates the cross-flow measuring plane with a pulsed laser light sheet. (See Figure 2 for a sketch of the SDPIV setup.) To enhance the illumination, the flow within the tunnel was seeded with smoke produced from a commercial smoke generator upstream of the tunnel's settling chamber. The sizes of seeding particles were typically ranged from 0.8 to 2 microns. Two high-resolution video cameras recorded simultaneous images through the windows on one side of the test section from two opposite angles and directions relative to the same measurement plane. As a result, all three components of velocity (i.e., streamwise (u), spanwise (v), and vertical (w)) were measured in each cross-flow plane through stereoscopic vector reconstruction [15]. Subsequently, instantaneous and mean velocity components were extrapolated from the data files. Two hundred frames of instantaneous data were obtained

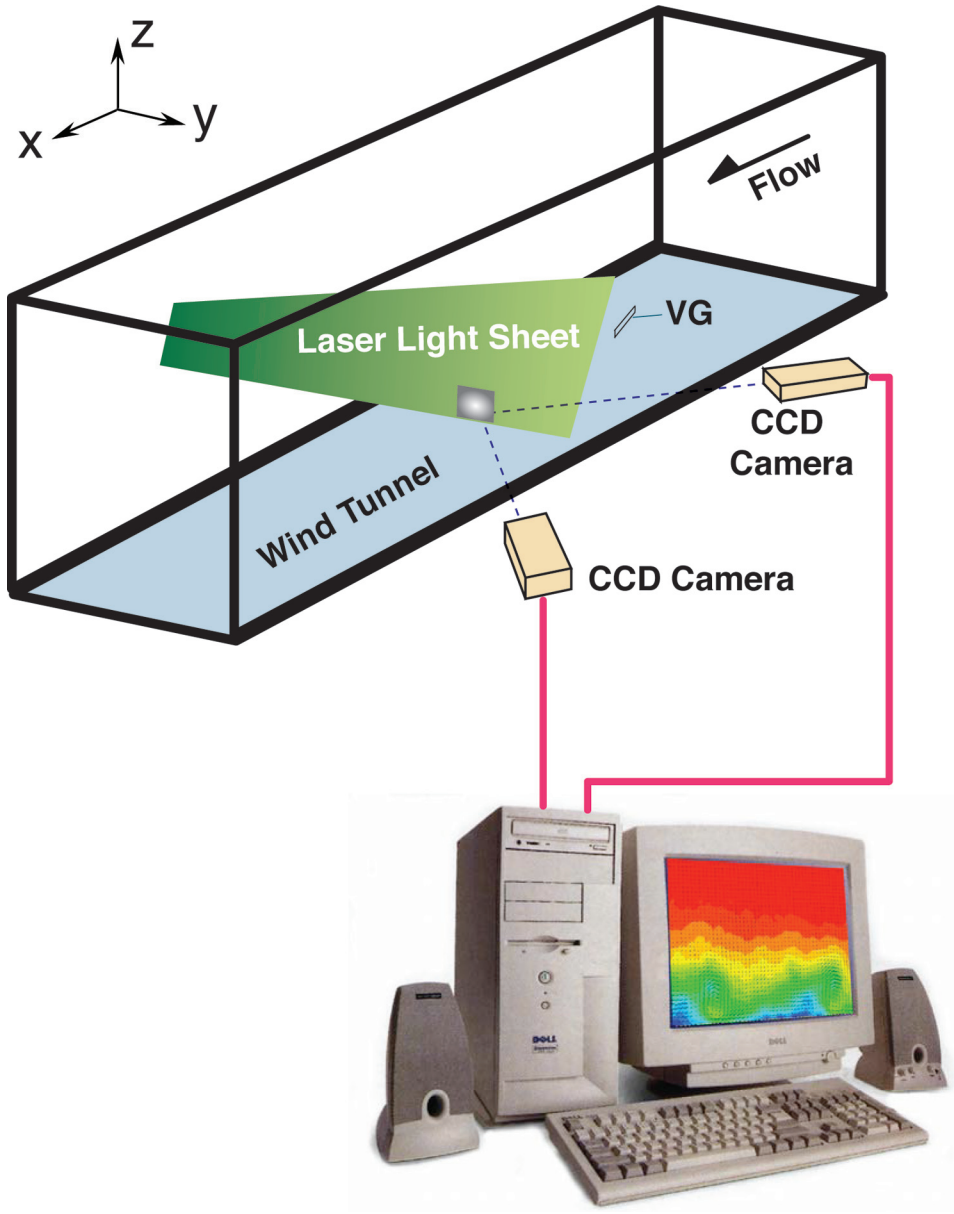

Figure 2. Schematic of SDPIV setup in wind tunnel.

and averaged for each set of mean results. Bad vectors were filled based on interpolations from the neighboring grids. The data dropout rate was less than 1%. Taking the data uncertainty and bias errors into account, the maximum error associate with the SDPIV measurement was estimated to be within ±2.5%.

The entire optical portion of the SDPIV system traversed to twelve different cross-flow (y-z) plane measuring stations downstream of the VG to acquire the flow-field data. The twelve measuring stations are listed in Table 1, represented by the streamwise distance between VG trailing edge and measuring station, Δx, and its nondimensionalized form, Δx/h. At each measurement location, the SDPIV field-of-view was approximately 85 mm in the spanwise (y) direction and 60 mm in the vertical (z) direction, near the tunnel centerline. The images from the cameras were carefully calibrated with an in situ target just before each measurement.

Table 1. Measurement stations for the cross-flow planes

Station No.	Δx (mm)	Low-profile VG Δx/h	Conventional VG Δx/h
1	6.78	0.97	0.19
2	13.85	1.98	0.40
3	21.24	3.04	0.61
4	26.94	3.86	0.77
5	35.34	5.06	1.01
6	69.61	9.97	1.99
7	105.56	15.11	3.02
8	121.84	17.44	3.49
9	349.25	50.00	10.00
10	764.53	109.45	21.89
11	1048.00	150.04	30.01
12	1397.00	200.00	40.00

3. RESULTS AND DISCUSSIONS

3.1 Flow-field Data: Mean Velocity Contours

The flow-field data measured by the SDPIV system for the low-profile VG and conventional VG are shown in Figures 3 and 4, respectively. The data are presented in terms of primary mean velocity (u) contours for all three angles of attack examined (i.e., 10°, 16°, and 23°), as well as at six selected downstream measuring stations that cover $3h \le \Delta x \le 109h$ for the low-profile VG and $1h \le \Delta x \le 40h$ for the conventional VG. The VG geometry projected onto each y-z plane is also shown.

When viewing toward the upstream direction (as in Figures 3 and 4), the vortex motion is counterclockwise for both VGs, where $y = 0$ represents the VG trailing-edge locations. For the low profile VG, the device leading edge was located at y = –8.5 mm for $\alpha = 10°$, y = –13.5 mm for $\alpha = 16°$, and y = –19.1 mm for $\alpha = 23°$. For the conventional VG, the leading edge was located at y = –12.1 mm for $\alpha = 10°$, y = –19.3 mm for $\alpha = 16°$, and y = –27.3 mm for $\alpha = 23°$. The figures show that the flow is swept upward on the windward side (+y direction) and downward on the leeward side (–y direction) of the VG.

For both VG cases, the velocity contours of Figures 3 and 4 show a velocity deficit in the vortex core that becomes more clearly defined as angle of attack is increased from 10° to 23°. For all three angles of attack, the boundary layer in the down-flow region is significantly thinned, as high momentum fluid is drawn toward the wall. On the opposite end, the low-momentum boundary-layer fluid is swept upward causing a slight thickening of boundary layer in the up-flow region. As expected, these effects are more pronounced for the conventional VG, which produced a stronger vortex and a more coherent structure, than for the low-profile VG.

The velocity contour figures also indicate that the initial formation of the streamwise vortex starts at the leeward side of the VGs (–y direction) as the boundary-layer flows are forced to curve over the device from the windward side to start the swirling process. Consequently, the vortex forms initially on the leeward side via conservation of angular momentum. This is slightly different than the commonly assumed vortex generation from the device trailing edge [14] (y = 0).

In order to adequately quantify vortex evolution, four parameters (vortex descriptors) were identified from past studies of the development of a streamwise vortex embedded in a turbulent boundary layer [12–14]. These parameters are peak streamwise vorticity ($\omega_{x,max}$), vortex circulation (Γ), location of the vortex core center, and half-life radius ($R_{0.5}$). The $\omega_{x,max}$ indicates vortex

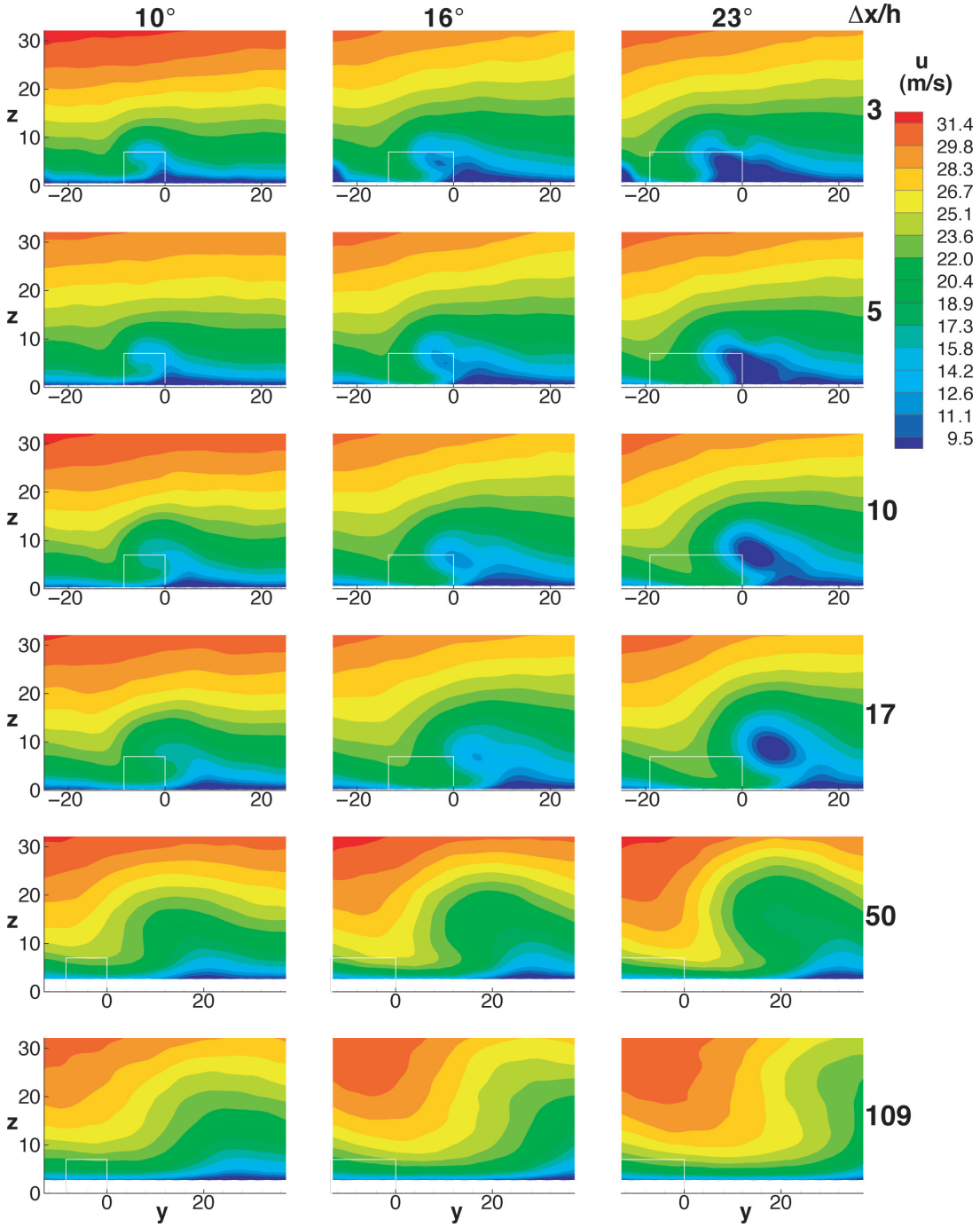

Figure 3. Mean velocity contours at 6 stations downstream of low-profile VG for α = 10°, 16°, and 23°.

concentration and is used to locate the center of the vortex core; vortex core location is used to determine the vortex trajectory; Γ represents the vortex "spinning" strength; and $R_{0.5}$ is directly related to vortex size. These four parameters properly describe the concentration, strength, path, and size of an embedded streamwise vortex and they are all extracted from the "vorticity data" in the downstream cross-flow planes. Thus, secondary velocity data (v, w) in the downstream y-z (cross flow) plane were used to compute the vorticity contours and their results are presented in the following discussions.

3.2 Vorticity Distributions

The contours of streamwise vorticity (ω_x), which more accurately depict development of the embedded streamwise vortex than the velocity contours, are illustrated in Figures 5 and 6 for both VGs at all three angles of attack examined, and for same set of measuring stations as in Figures 3 and

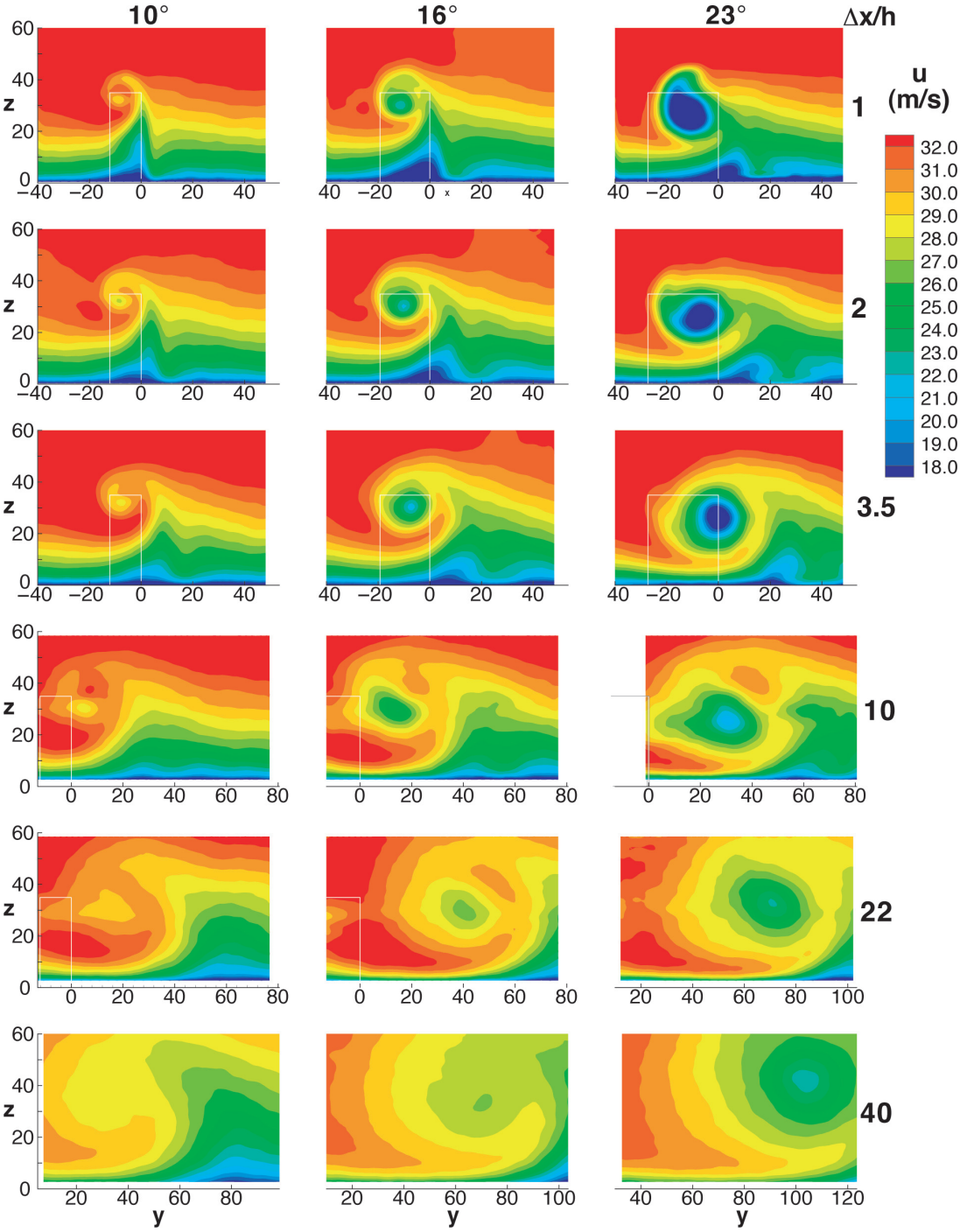

Figure 4. Mean velocity contours at 6 stations downstream of conventional VG for α = 10°, 16°, and 23°.

4 for each respective VG. The VG shape projected onto each cross-flow plane is also shown for reference.

In all cases, the vorticity contours indicate a fairly concentrated vortex structure within $\Delta x \leq 20h$. For the low-profile VG, the vorticity contours of Figure 5 show that the maximum vorticity decays rapidly and the vortex cores become more diffused for $\Delta x \geq 20h$ (Station 8) where the vortex core became less well-defined and the primary vorticity no longer seems to dominate the flow field. Beyond $\Delta x = 109h$ (Station 12, not shown), the vorticity becomes virtually nonexistence, whereas for the conventional VG, the vortex has a more circular shape and decays at a slower rate such that its vortical structure remains well-defined at the farthest downstream station of $\Delta x = 40h$ (Station 12). The higher decay rate of vorticity for the low-profile VG is probably caused by the trailing vortex being much

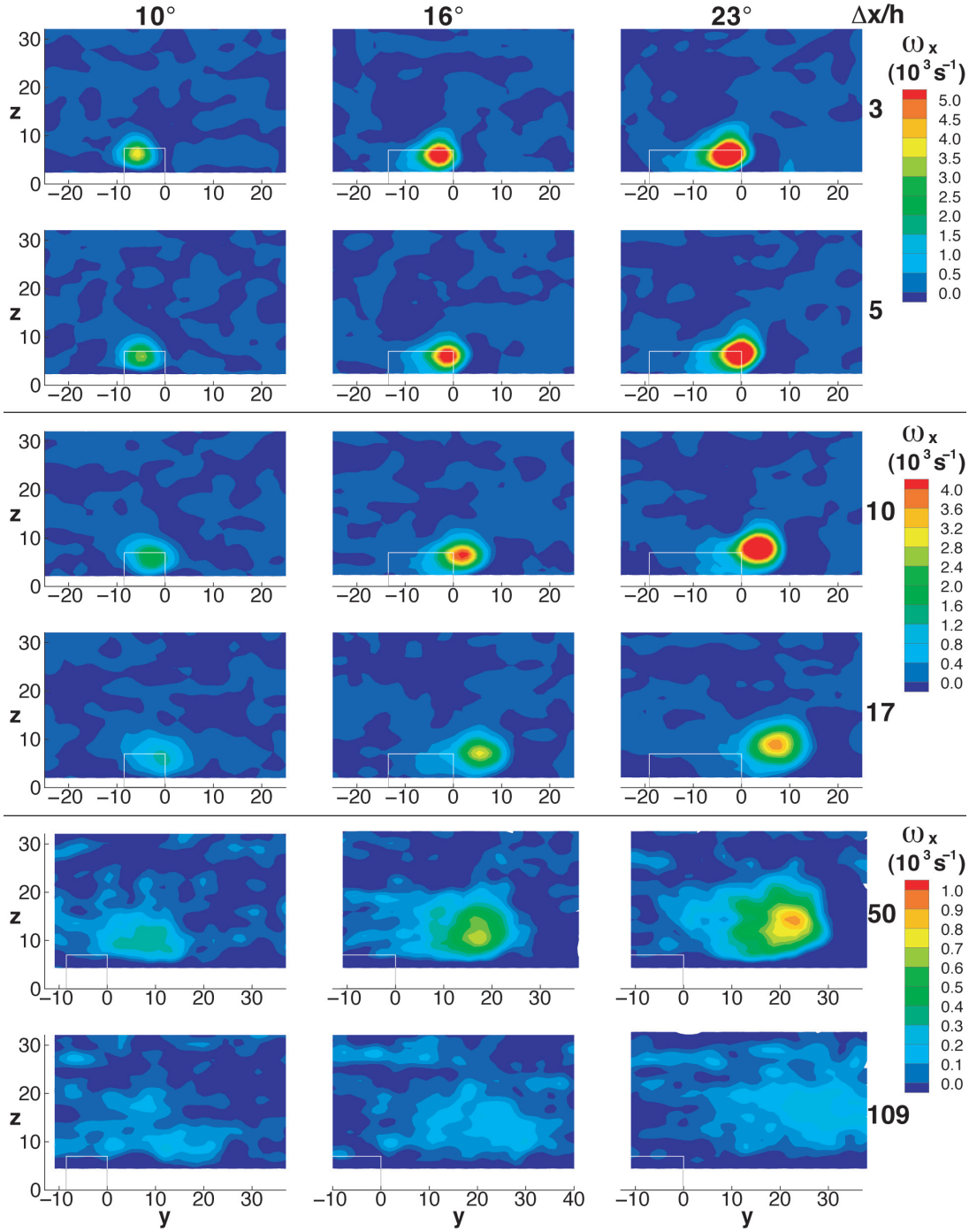

Figure 5. Mean vorticity contours at 6 stations downstream of low-profile VG for α = 10°, 16°, and 23°.

closer to the wall, as indicated by the slightly oval shape of its vortical structure, and the vortex dissipation process being enhanced by the resulting higher shear flow.

To better illustrate vortex decay, the streamwise distribution of peak vorticity, $\omega_{x,max}$, is plotted as a function of nondimensionalized downstream distance, $\Delta x/h$, for all cases examined (see Figures 7(a) and 7(b)) where $\Delta x/h = 0$ is the VG trailing-edge location. The vortex decay plot confirms the results from the velocity and vorticity contours where the peak vorticity is rapidly attenuated downstream of the low-profile VG for all three angles of attack examined. The peak vorticity decayed exponentially to Δx such that it decreased by almost a factor of 10 within the initial 50h downstream. Similar trends were also observed for the conventional VG with angles of attack of 10° and 16° for up to 40h

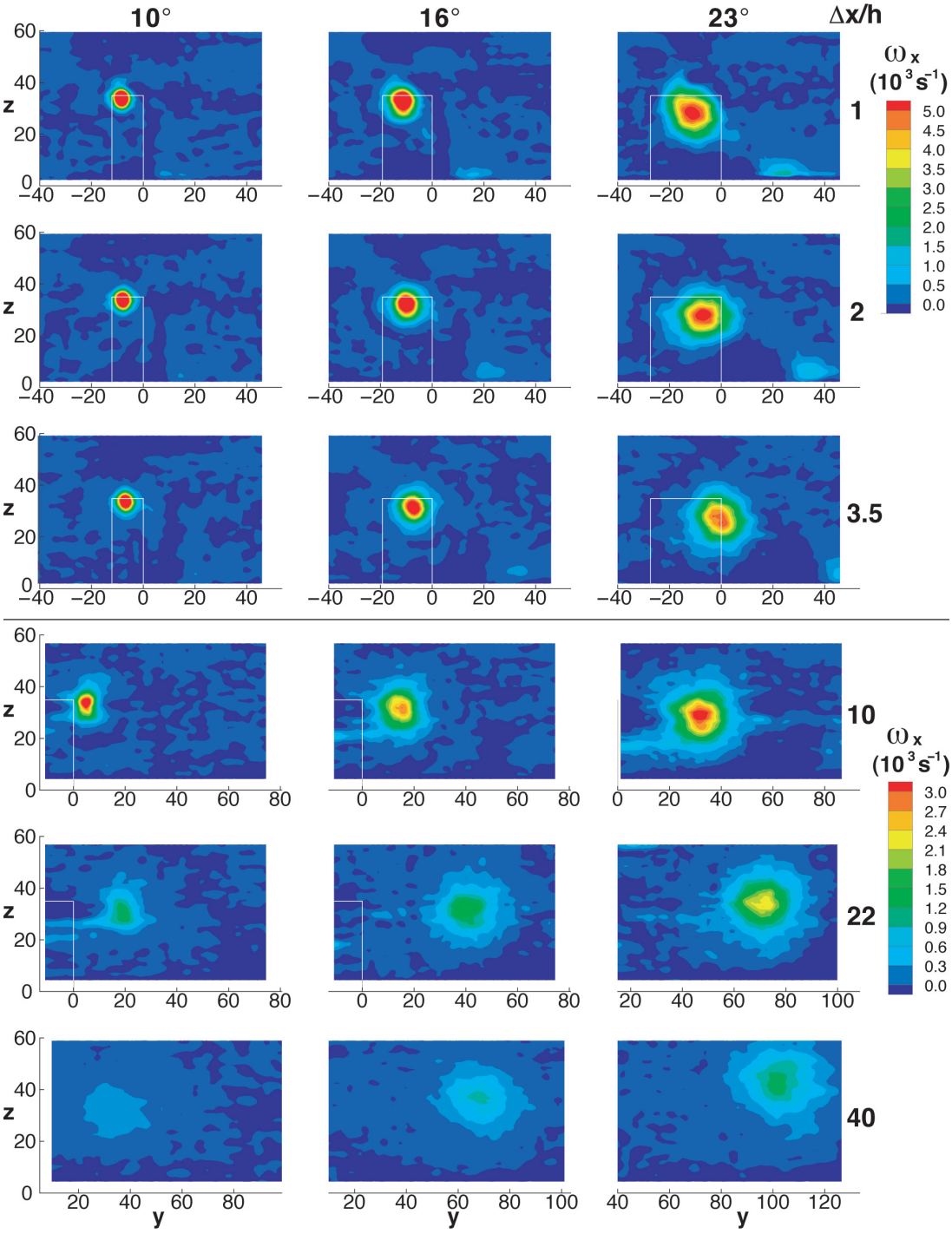

Figure 6. Mean vorticity contours at 6 stations downstream of conventional VG for α = 10°, 16°, and 23°.

downstream. Notice that the error bars (±2.5%) are not shown in this and subsequent figures, because the bars were all on the order of or less than the size of the symbols.

As expected, the magnitude of $\omega_{x,max}$ increases as angle of attack increases for the low-profile VG (Figure 7(a))—an increase that is roughly a function (ratio) of sin(α). Somewhat surprising is the result of the conventional VG, where the trend of peak vorticity is reversed (Figure 7(b)). Immediately downstream of the device, the maximum vorticity occurred at α = 10°, or at about the same level as that of the low-profile VG at α = 23° (i.e., $\omega_{x,max} \approx 11 \times 10^3$ 1/s). The peak vorticity reduced by about 13% for α = 16°; but for α = 23°, an unexpected reduction of almost 50% occurred. Because of the lower initial vorticity and lower decay rate, the peak vorticity data of the conventional VG at α = 23°

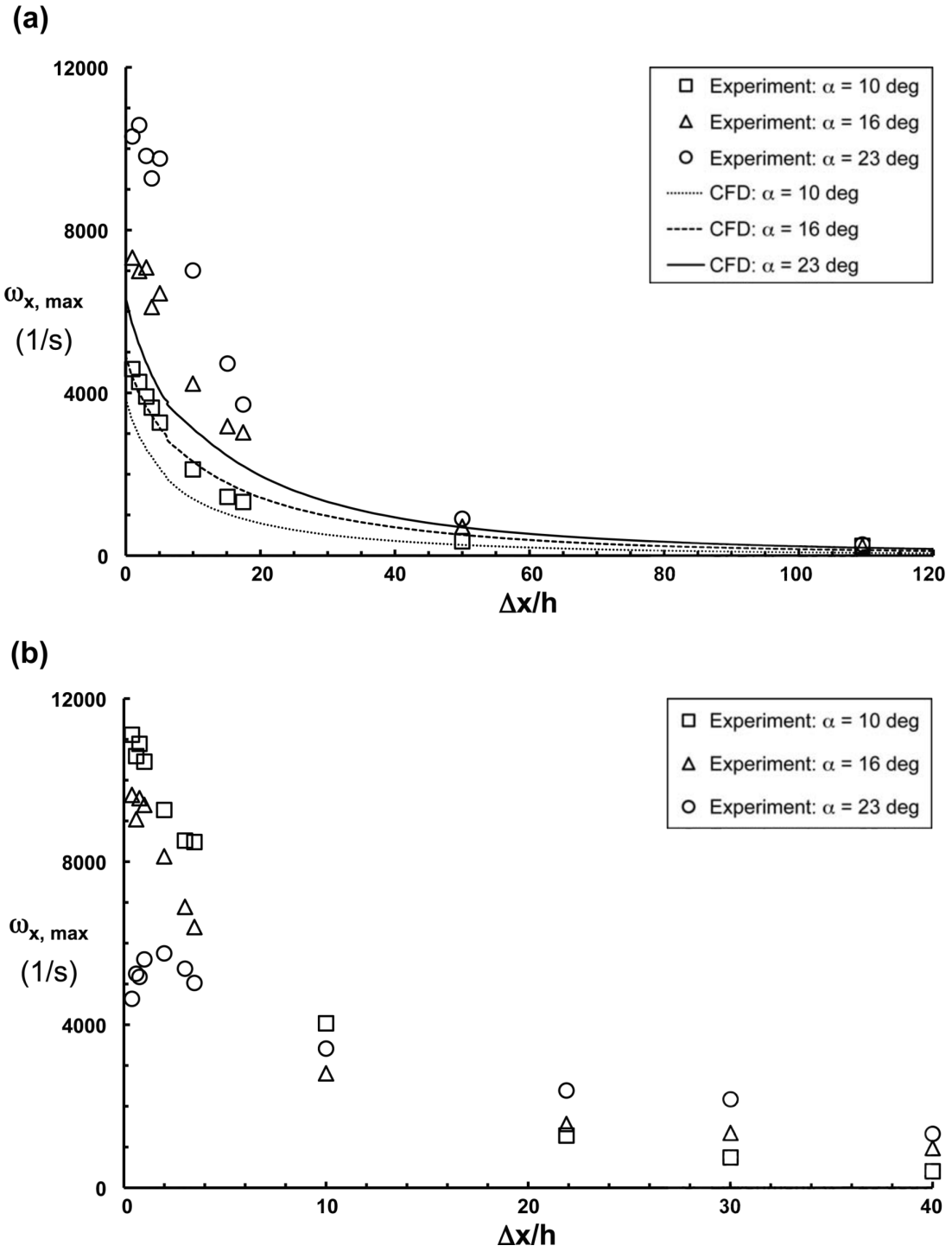

Figure 7. Decay of peak vorticity for VGs at α = 10°, 16°, and 23°; (a) Low-profile VG, (b) Conventional VG.

"crossed-over" the paths of the other two angles of attack and achieved the highest peak vorticity for locations beyond $\Delta x \approx 15h$.

It is hypothesized that the flow around the conventional VG might be slightly stalled at $\alpha = 16°$ and severely stalled at $\alpha = 23°$ because the device-induced vortex covers only a small portion of the VG vertically near its tip region at the two higher angles of attack (Figure 6). On the other hand, the low-profile VG produces a vortex that covers the entire device vertically (Figure 5). Combining this fact with the substantially higher turbulence intensity and flow mixing that naturally occurred near the wall (i.e., $h/\delta \approx 0.2$) enables the smaller VG to reach a much higher angle of attack without the flow being stalled. This could explain the phenomenon of "trend reversal of peak vorticity" for the conventional

VG and why the low-profile VG produces a value that is double that of the larger VG just downstream of the device for $\alpha = 23°$.

Experimental results for the low-profile (smaller) VG were also compared with an existing set of CFD predictions that was reported by Allan et al. [16]. The numerical simulations were performed using the NASA OVERFLOW code [17] and the two-equation (k-ω) Shear-Stress Transport (SST) model of Menter [18], which an initial CFD study had shown to perform the best. The SST model accounts for the transport of the principal shear stress in adverse pressure gradient boundary layers. The flow domain was discretized using five million grid points, which included the flow from the leading edge of the flat plate. Grid convergence studies indicated that the numerical simulation results were converged in both streamwise and cross-flow directions [16].

The main goal of the CFD effort has been to develop effective but simplified boundary conditions in device-based models, as described by Bender [19]. The low-profile VG shares more similarities with the active flow-control devices of current interest than the conventional VG, such as using the approach of "minimal" near-wall protuberances, and is thereby more relevant for the development of simpler actuator models (i.e., faster and easier to use) for CFD predictions.

Figure 7(a) compares CFD prediction of $\omega_{x,max}$ with those of experiments for the low-profile VG. Although CFD results confirm the rapid decay of peak vorticity for most angles of attack examined, the vorticity magnitude and its decay rate closer to the device (i.e., $\Delta x < 20h$) were not accurately predicted by CFD. The largest discrepancies occurred for the $\alpha = 23°$ case, where CFD tends to underpredict the magnitude of peak vorticity closer to the device by as much as 40%. This is perhaps due to the smearing of the peak vorticity through turbulent/numerical dissipation in the CFD modeling.

3.3 Vortex Circulation

The vortex circulation discussed in this section is the positive circulation (Γ_p), which was first determined by finding the vortex core location from the vorticity contour plots, then by integrating the positive (dominant) streamwise vorticity over the area surrounding the vortex core in the y-z plane. Figure 8 illustrates the resulting streamwise distribution of vortex circulation.

As expected, the circulation increases as angle of attack increases for both VGs examined—an increase that is roughly a function of $(\sin(\alpha))^{1.5}$, particularly for locations immediately downstream of the device. The vortex strength of conventional VG (Figure 8(b)) is roughly four times larger than that of the low-profile VG for the same angle of attack (Figure 8(a)). In comparison with the decay of peak vorticity, the circulation decay is more linear, especially for the conventional VG. Circulation decays by approximately a factor of 3 over a distance of about 100h for the low-profile VG, and by almost a factor of 2 over a distance of 40h for both VGs at $\alpha = 23°$.

The trends for circulation decay follow roughly a similar path, with the higher angle of attack cases decaying at slightly higher rates. This is probably because of the associated larger wall shear since a major contributor to circulation decay is the action of wall friction that induces a lateral component of wall shear stress opposing the vortex rotation.

Unlike the prediction of $\omega_{x,max}$, the CFD accurately predicted Γ_p for $\Delta x < 20h$, mostly within 5% of the experimental results. CFD predicted a larger but less concentrated vortex than the experimental results; however, when integrating a smaller ω_x over a larger area (to be shown later under discussions of vortex size), the two discrepancies canceled one another, resulting in accurate predictions for Γ_p. Perhaps the circulation production is more of an inviscid-dominated process and thereby less difficult to predict computationally than that of the viscous-dominated peak vorticity.

3.4 Vortex Path

By observing the vortex center (or core) location as a function of downstream location (Δx), one can determine the experimental vortex path in both lateral (y) and vertical (z) directions, as shown in Figures 9(a) and 9(b) for both VGs at the three angles of attack examined. All coordinates are nondimensionalized by the h of each respective VG. The vorticity contours of Figure 5 show the presence of significant experimental uncertainty in defining the vortical structure that determines the vortex center for the low-profile VG at $\Delta x = 109h$ (Station 10); therefore, the vortex path results are presented only for $\Delta x \leq 50h$ (i.e., up to Station 9).

The initial lateral path of the vortex tends to follow the general direction that the trailing edge of the device is pointed towards (Figure 9(a)). Although significantly diminished, this tendency still persists for both low-profile and conventional VGs at the farthest measuring stations downstream (i.e., $\Delta x =$ 109h and 40h, respectively). Figure 9(a) shows that the trajectory in the lateral direction increases

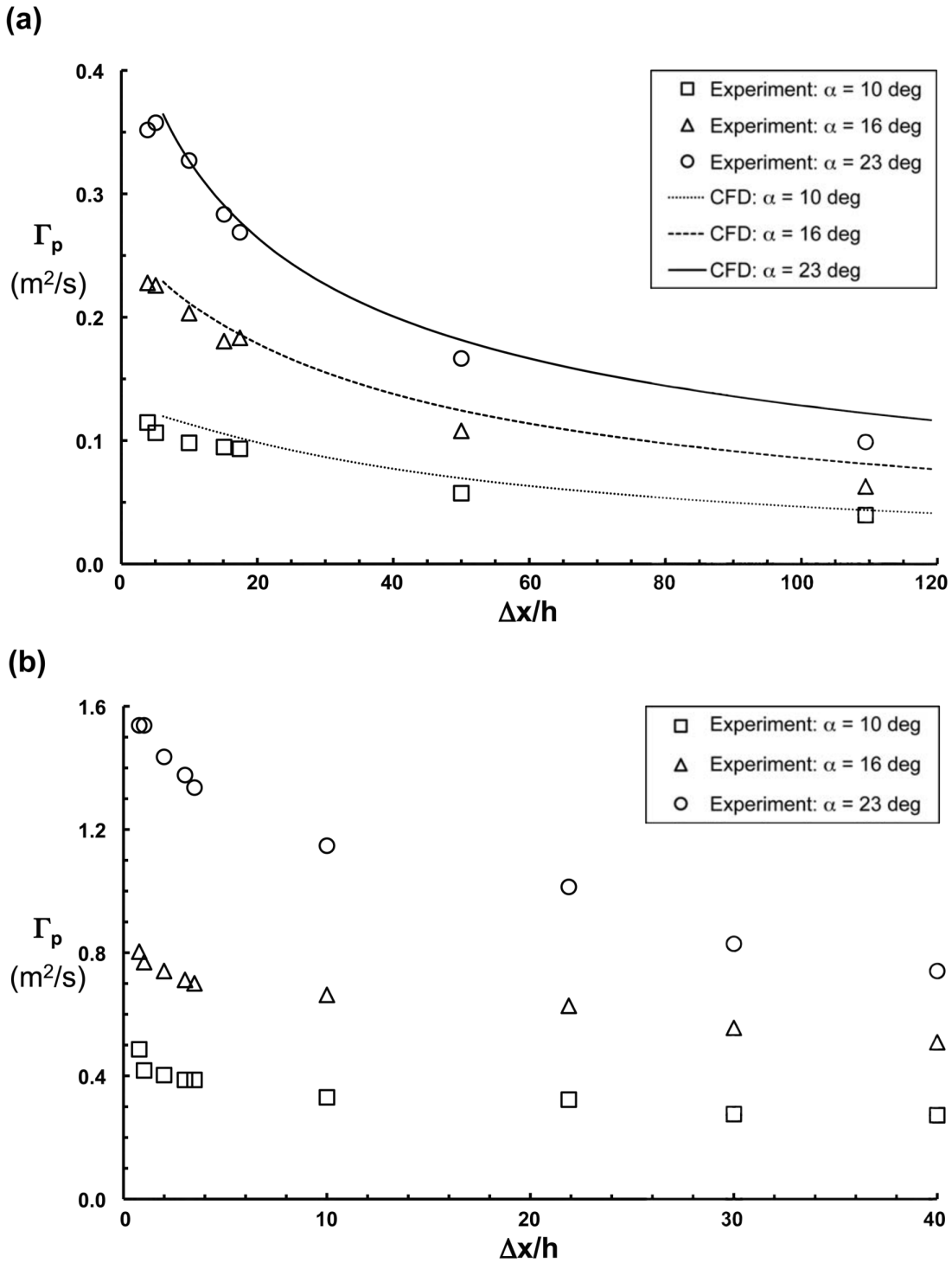

Figure 8. Circulation for VGs at α = 10°, 16°, and 23°; (a) Low-profile VG, (b) Conventional VG.

proportionally as angle of attack increases and the nondimensionalized trajectory paths roughly parallel one another between the two VGs.

The vertical path of both VGs stays roughly on the order of the device height (between 0.7h and 1.2h) except for the case of the low-profile VG at α = 23°. In this case, the slope of the vertical trajectory is significantly higher than all other cases, which results in flow mixing almost twice in height as the vortex travels downstream (see Figure 9(b)). The larger vortex core near the wall results in a significantly greater interaction with the wall, which is probably the reason behind this

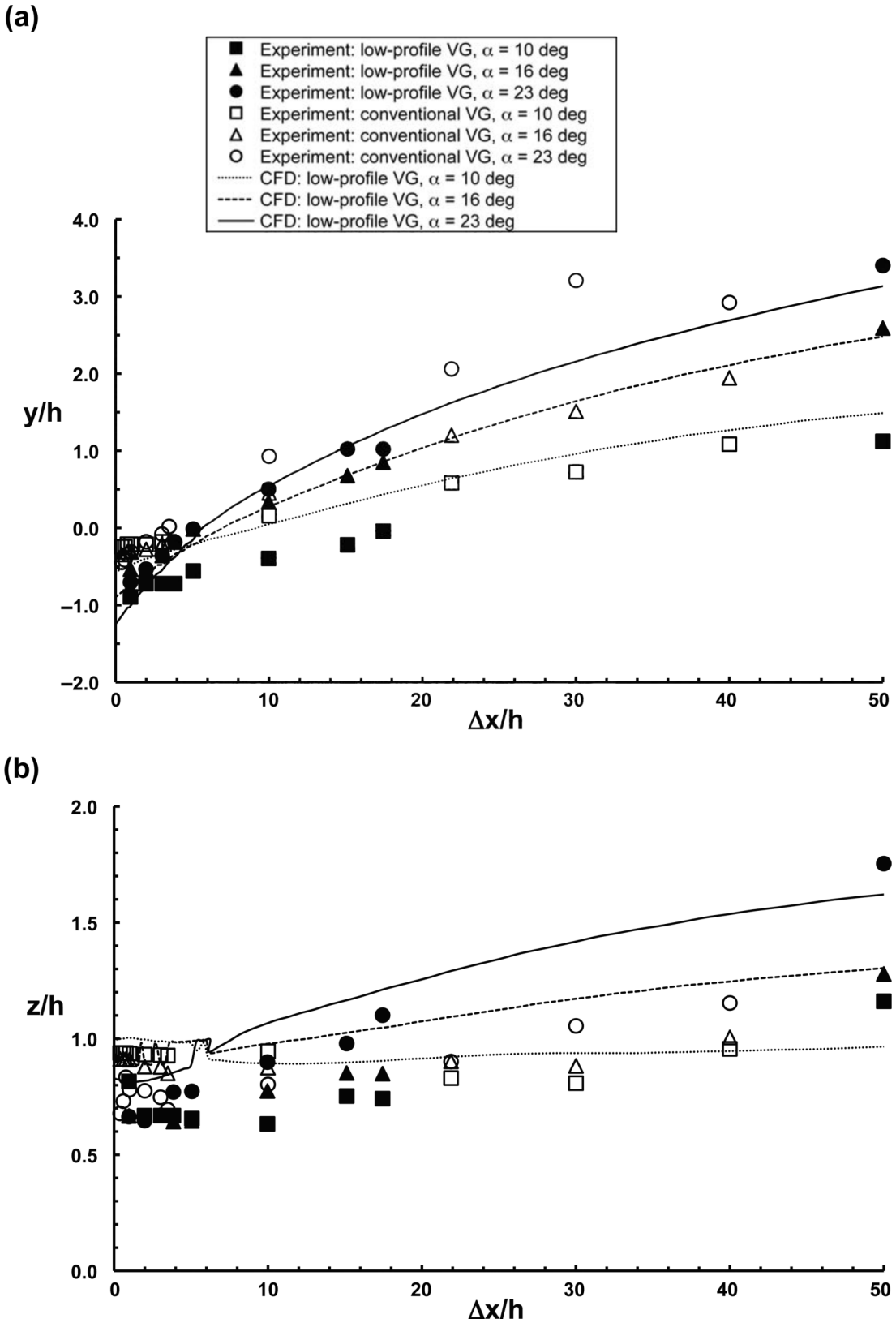

Figure 9. Vortex paths nondimensionalized by device height; (a) Spanwise trajectory, (b) Vertical trajectory.

phenomenon. Nevertheless, the device-height normalized vortex paths, especially in the lateral direction, for the low-profile VG generally follow the same trends for the conventional VG.

Figure 9 also presents the experimental results for comparison with the CFD predictions. For the most part, the CFD results of the lateral and vertical paths are in reasonably good agreement with the experimental data, with the former being more accurately predicted.

3.5 Vortex Size: Half-life Radius

The vortex size was investigated in terms of a "half-life" radius, $R_{0.5}$. The half-life radius is defined as the radial distance from the center of the vortex core where the local vorticity was equal to half the peak vorticity. In this region, $R_{0.5}$ could be determined more accurately because there was no difference between the experimental trends and the Gaussian distribution shape described by Bray [14]. Consequently, circulation could be estimated from peak vorticity and half-life radius using:

$$\Gamma = (\omega_{x,max}\pi R_{0.5}{}^2)/0.693$$

Since the shape of the vortex was not always perfectly circular, $R_{0.5}$ was approximated by averaging its values in the vertical and lateral directions. The values of $R_{0.5}$ are then normalized by h and plotted against the nondimensionalized downstream distance in Figure 10(a). Again, because of significant uncertainty in defining the vortical structure that determines the vortex radius for the low-profile VG at $\Delta x = 109h$ (Figure 5), the results of $R_{0.5}$ are presented only for $\Delta x \leq 50h$.

Although there exists some scattering of the experimental data, the nondimensionalized half-life radius seems independent of angle of attack and is growing virtually linearly for $\Delta x \leq 50h$. This independence of radius on angle of attack is probably caused by the vortex's close vicinity to the wall during its initial formation, and thus h becomes the limiting parameter for the vortex size instead of the projected chord length (i.e., $e(\sin(\alpha))$).

CFD results overpredicted $R_{0.5}$ by up to 40 percent for the low-profile VG with $\Delta x < 20h$. Like the difficulty encountered in predicting the peak vorticity, the inaccuracies in size prediction are probably related to numerical scheme and/or modeling issues associated with the computation of turbulence diffusion. Nevertheless, CFD predicted (and confirmed) the linear increase of radius that is virtually independent of α for $\Delta x \geq 10h$ as the vortex evolves downstream.

For the conventional VG, the physical dimension of radius is about three times that of the low-profile VG at $\alpha = 23°$. Again, the half-life radius of the larger VG is normalized by h, as shown in Figure 10(b). The figure shows that the radius of the conventional VG at $\alpha = 23°$ is initially over twice that of its two lower angles of attack initially, but drops off to the level of the latter ones for $\Delta x \geq 30h$. This is a trend that is generally opposite to the VG's peak vorticity distributions (Figure 7(b)). The rate of vortex expansion is the highest for the $\alpha = 10°$ case, followed by the cases for $\alpha = 16°$ and 23°, respectively.

In contrast to the low-profile VG, the radius of the conventional VG is more dependent on angle of attack, since the wall is relatively farther away and therefore not able to restrict the initial growth of the vortex. Thus, the $R_{0.5}$ data roughly "collapsed" together for $x/h \leq 10$ by normalizing with the projected device chord length, $e(\sin(\alpha))$, as shown in Figure 11. Farther downstream ($x/h > 10$), the data diverge as the diffusion process dominates.

4. CONCLUSIONS

The experimental database for a device-induced streamwise vortex was enhanced by detailed flow-field measurements via a SDPIV system downstream of a single vane-type VG embedded within a flat-plate turbulent boundary layer in the Langley 20- by 28-Inch Shear Flow Tunnel. In-depth analysis was made for the flow field produced by a low-profile VG and a conventional VG in order to gain a better physical understanding of the vortex development process. Parameters that describe the vortex concentration, strength, path, and size were extracted from the vorticity data. Comparisons were made with an existing set of CFD predictions for the low-profile VG.

Key results are summarized as follows:

1. The maximum vorticity magnitude increases as angle of attack increases for the low-profile VG, but the trend is reversed for the conventional VG, probably due to the flow being partially stalled or stalled around the larger VG at higher angles of attack.

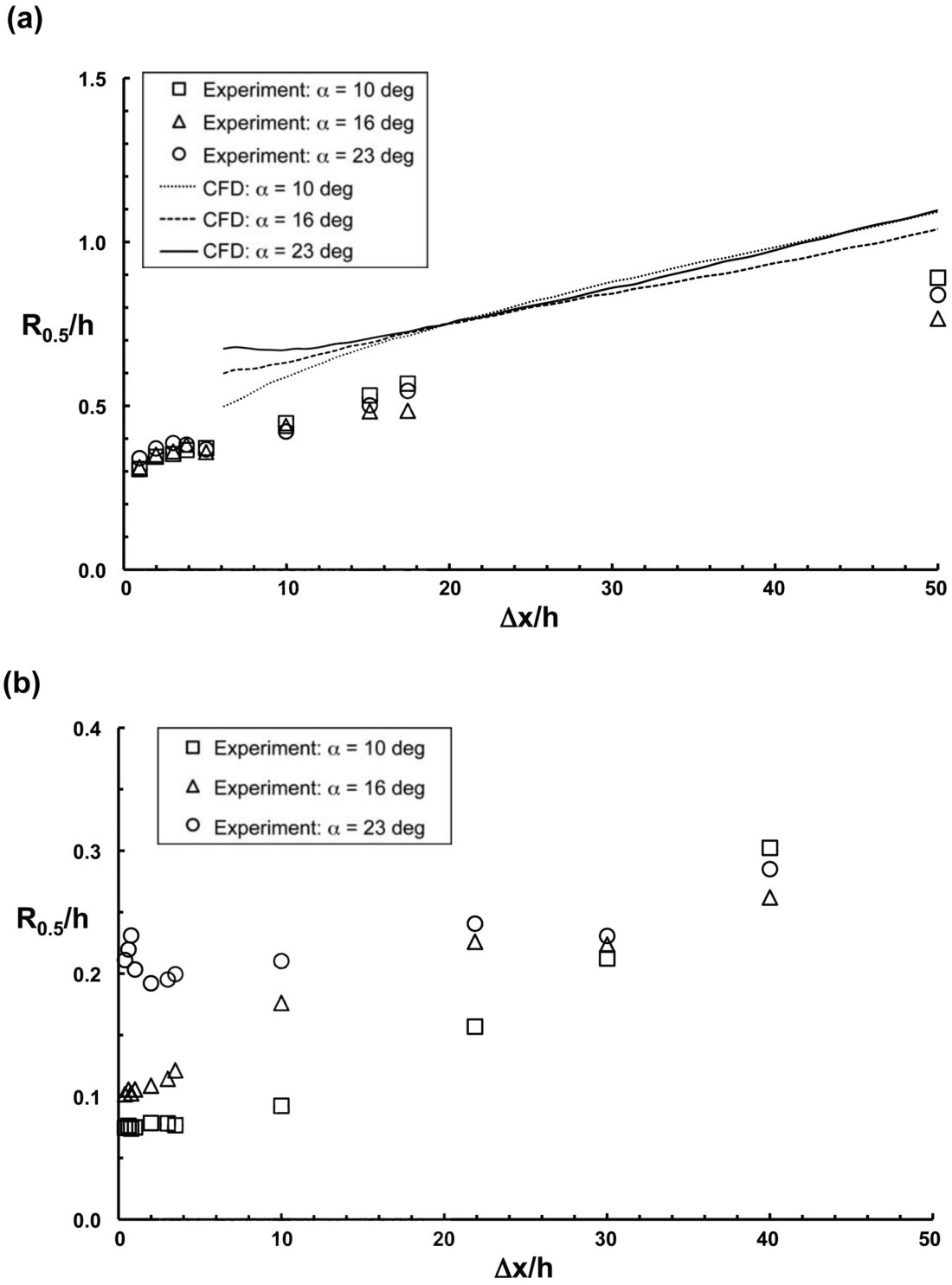

Figure 10. Vortex half-life radius nondimensionalized by device height; (a) Low-profile VG, (b) Conventional VG.

2. Peak vorticity for the low-profile VG decays exponentially to Δx such that it decreased by almost a factor of 10 within the initial 50h downstream, while circulation decay is more linearly proportional to Δx.
3. The device-height normalized vortex trajectories for the low-profile VG, especially in the lateral direction, follow the general trends of the conventional VG.
4. An existing set of CFD results predicted the vortex circulation and path well, but under-predicted the peak vorticity and over-predicted vortex radius.

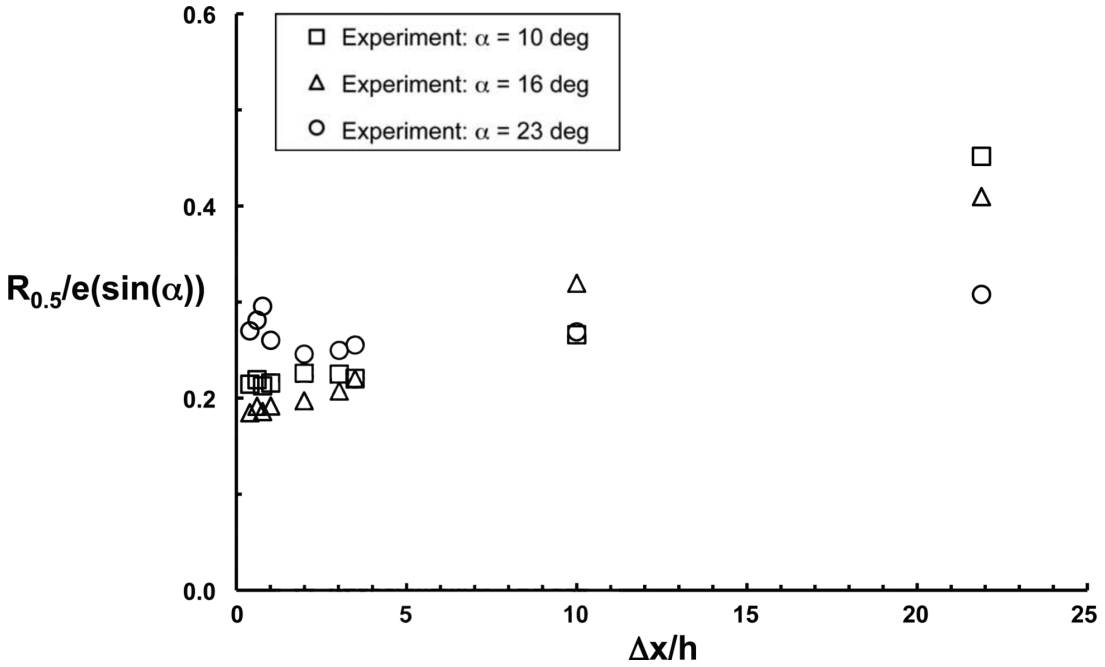

Figure 11. Vortex half-life radius of conventional VG nondimensionalized by projected device chord length.

The high rate of vorticity decay for the low-profile VG might have important flow-control implications, such as for applications associated with an S-duct type of compact engine inlet where the rapid attenuation of streamwise vortices is highly desirable once the short-range flow-control objective is achieved.

REFERENCES

1. Taylor, H. D., "The Elimination of Diffuser Separation by Vortex Generators," United Aircraft Corporation Report No. R-4012-3, June 1947.
2. Schubauer, G. B., and Spangenber, W. G., "Forced Mixing in Boundary Layers," *Journal of Fluid Mechanics*, Vol. 8, Part 1, 1960, pp. 10–32.
3. Pearcey, H. H., "Shock Induced Separation and Its Prevention by Design and Boundary-Layer Control," *Boundary Layer and Flow Control*, Vol. 2, ed. G. V. Lachman, Pergamon Press, New York, 1961, pp. 1166–1344.
4. Lin, J. C., Howard, F. G., and Selby, G. V., "Small Submerged Vortex Generators for Turbulent Flow Separation Control," *Journal of Spacecraft and Rockets*, Vol. 27, No. 5, Sept.-Oct. 1990, pp. 503–507.
5. Holmes, A. E., Hickey, P. K., Murphy, W. R., Hilton, D. A., "The Application of Sub-Boundary Layer Vortex Generators to Reduce Canopy Mach Rumble Interior Noise on the Gulfstream III," AIAA Paper 87-0084, Jan. 1987.
6. Lin, J. C., Robinson, S. K., McGhee, R. J., and Valarezo, W. O., "Separation Control on High-Lift Airfoils Via Micro-Vortex Generators," *Journal of Aircraft*, Vol. 31, No. 6, Nov.-Dec. 1994, pp. 1317–1323.
7. Jenkins L, Gorton S. A, Anders S., "Flow control device evaluation for an Internal Flow with an adverse pressure gradient," AIAA Paper 2002-0266, Jan. 2002.
8. Ashill, P. R., Fulker, J. L., and Hackett, K. C., "Research at DERA on Sub Boundary Layer Vortex Generators (SBVGs)," AIAA Paper 2001-0887, Jan. 2001.
9. Ashill P. R, Fulker J. L, Hackett, K. C., "Studies of flows induced by Sub Boundary layer Vortex Generators (SBVGs)," AIAA Paper 2002-0968, Jan. 2002.
10. Hamstra, J. W., Miller, D. N., Truax, P. P., Anderson, B. H., and Wendt, B. J., "Active Inlet Flow Control Technology Demonstration," ICAS-2000-6.11.2, *22nd International Congress of the Aeronautical Sciences*, Aug.-Sept. 2000.

11. Anderson, B. H., Miller, D. N., Yagle, P. J., and Truax, P. P., "A Study on MEMS Flow Control for the Management of Engine Face Distortion in Compact Inlet Systems," ASME Paper FEDSM99-9620, *Proceedings of the 3rd ASME/JSME Joint Fluids Engineering Conference*, July 1999.
12. Westphal, R. V., Pauley, W. R. and Eaton, J. K., "Interaction Between a Vortex and a Turbulent Boundary Layer-Part I: Mean Flow Evolution and Turbulence Properties," NASA TM 88361, Jan. 1987.
13. Wendt, B. J., Greber, I., and Hingst, W. R., "The Structure and Development of Streamwise Vortex Arrays Embedded in a Turbulent Boundary Layer," *AIAA Paper 92-0551*, Jan. 1992.
14. Bray, T. B., "A Parametric Study of Vane and Air-Jet Vortex Generators," EngD Dissertation, Cranfield Univ., UK., Oct. 1998.
15. Lourenco, L. M., and Krothapalli, A., "True Resolution PIV: A Mesh-Free Second Order Accurate Algorithm," *Proceedings of the 10th International Symposium on Application Techniques in Fluid Mechanics*, Lisbon, July 2000.
16. Allan, B. G., Yao, C-S, and Lin, J. C., "Numerical Simulations of Vortex Generator Vanes and Jets on a Flat Plate," AIAA Paper 2002-3160, June 2002.
17. Buning, P. G., Jespersen, D.C., Pulliam, T. H., Klopfer, W.M., Chan, W.M., Slotnick, J.P., Krist, S.E., and Renze, K.J., "OVERFLOW User's Manual Version 1.8m," NASA Langley Research Center, Jan. 2000.
18. Menter, F., "Improved Two-Equation Turbulence Models for Aerodynamic Flows," NASA TM 103975, 1992.
19. Bender, E. E., Anderson, B. H., and Yagle, P. J., "Vortex Generator Modeling for Navier-Stokes Codes," ASME Paper FEDSM99-6919, July 1999.